Diffraction gratings with two-orders-of-magnitude-enhanced dispersion rates for sub-meV resolution soft X-ray spectroscopy

Yuri Shvyd'ko*

Advanced Photon Source, Argonne National Laboratory, Argonne, IL 60439, USA.
*Correspondence e-mail: shvydko@anl.gov

Diffraction gratings with large angular dispersion rates are central to obtaining high spectral resolution in grating spectrometers operating over a broad spectral range from infrared to soft X-ray domains. The greatest challenge is of course to achieve large dispersion rates in the short-wavelength X-ray domain. Here it is shown that crystals in non-coplanar asymmetric X-ray Bragg diffraction can function as high-reflectance broadband soft X-ray diffraction gratings with dispersion rates that are at least two orders of magnitude larger than those that are possible with state-of-the-art man-made gratings. This opens new opportunities to design and implement soft X-ray resonant inelastic scattering (RIXS) spectrometers with spectral resolutions that are up to two orders of magnitude higher than what is currently possible, to further advance a very dynamic field of RIXS spectroscopy, and to make it competitive with inelastic neutron scattering. Examples of large-dispersion-rate crystal diffraction gratings operating near the 930 eV L_3 absorption edge in Cu and of the 2.838 keV L_3-edge in Ru are presented.

1. Introduction

Diffraction gratings are the most common type of light-dispersing optical elements. They are essential for optical instruments that operate in a very broad spectral range from infrared to soft X-ray domains. The shorter the radiation wavelength, the more challenging it is to manufacture efficient diffraction gratings. Diffraction gratings are typically not practical at photon energies E above 2 keV, but they are still very useful at lower photon energies in the soft X-ray domain, $0.2\,\text{keV} \lesssim E \lesssim 2\,\text{keV}$. They are key optical elements of resonant inelastic X-ray scattering (RIXS) spectrometers.

RIXS studies in the soft X-ray domain recently increased tremendously in importance because researchers discovered that it is possible to observe and study orbital and magnetic excitations in addition to charge and lattice collective excitations in condensed matter, notably in high-T_c superconductors (Braicovich et al., 2010; Tacon et al., 2011; Schlappa et al., 2012; Dean et al., 2013) previously accessible only by neutrons. This breakthrough became possible because of rapid improvements in the spectral resolution ΔE of RIXS spectrometers at synchrotron radiation facilities worldwide, initially from $\Delta E \simeq 120\,\text{meV}$ (Ghiringhelli et al., 2006; Strocov et al., 2010), achieved at SLS in 2006 to recently demonstrated resolutions of $\Delta E \simeq 40\,\text{meV}$ at ESRF (Chaix et al., 2017; Brookes et al., 2018) and $\Delta E \simeq 20\,\text{meV}$ at NSLS-II (Bisogni, 2019). Various facilities, such as ALS (Warwick et al., 2014; Chuang et al., 2017), TLS (Lai et al., 2014), DLS (Zhou, 2019),

MAX IV, European XFEL, and LCLS-II are now constructing new soft RIXS beamlines and spectrometers, aiming to achieve higher throughput and higher resolution. A RIXS spectrometer at NSLS-II has been designed to achieve a spectral resolution of $\Delta E \simeq 15$ meV and resolving power $E/\Delta E \simeq 6.6 \times 10^4$ (Dvorak *et al.*, 2016).

However, to become competitive with inelastic neutron scattering, the resolution of the RIXS spectrometers must be improved by more than an order of magnitude. Technically, the progress in the spectral resolution of RIXS became possible due to better focusing of X-rays, improved spatial resolution of X-ray detectors, and most importantly by increasing the length of the spectrometer arm from 5 m (Ghiringhelli *et al.*, 2006) to 15 m (Dvorak *et al.*, 2016). However, the potential to further improve spectral resolution by increasing spectrometer sizes is approaching obvious limits.

A more promising approach would be to improve the angular dispersion rate of the diffraction gratings, which is central to achieving high spectral resolution of grating monochromators, spectrometers, and other devices. In addition, large angular dispersion rates may counteract insufficient detector spatial resolution and large slope errors. (see Appendix *A*).

Angular dispersion rate $\mathcal{D}$ measures the angular variation of the propagation direction of the diffracted photon with its energy. It is primarily determined by the smallness of the diffraction grating period, or equivalently by the large value of the groove density g. The maximum angular dispersion rates of the state-of-the-art diffraction gratings is in the range $\mathcal{D} \simeq 0.2$–0.4 µrad meV^{-1} at $E \simeq 1$ keV, corresponding to a groove density of $g \simeq 5$–10 µm^{-1} (Michette, 1986; Ghiringhelli *et al.*, 2006; Strocov *et al.*, 2010; Chaix *et al.*, 2017; Brookes *et al.*, 2018; Bisogni, 2019; Warwick *et al.*, 2014; Chuang *et al.*, 2017; Lai *et al.*, 2014; Zhou, 2019; Dvorak *et al.*, 2016; Voronov *et al.*, 2014, 2015).

However, nobody can make better gratings than nature. The 'groove' density of atomic planes in crystals can be as large as one per crystal lattice period, which is $\gtrsim 1$ nm^{-1}, *i.e.* at least two orders of magnitude larger than what is currently possible with man-made gratings. If crystal gratings with atomic groove density could be efficiently used, this would lead to much higher dispersion rates and higher-resolution optical devices.

Indeed, the grating effect of angular dispersion of X-rays in Bragg diffraction from a crystal can be realized, but only under conditions of asymmetric diffraction, in which the diffracting atomic planes are at a nonzero asymmetry angle η to the entrance crystal surface. The effect of angular dispersion in Bragg diffraction was discussed in detail (Shvyd'ko, 2004), experimentally demonstrated in the hard X-ray regime in coplanar scattering geometry (Shvyd'ko *et al.*, 2006), and applied to inelastic X-ray scattering spectrometers with sub-meV resolution in the hard X-ray domain (Shvyd'ko *et al.*, 2014; Chumakov *et al.*, 2019). Nothing prevents using this approach in the soft X-ray domain, given crystals with large lattice parameter are available. But, a direct copy of such an approach results in low-efficient (narrowband and low-

reflectance) Bragg-diffraction crystal gratings as pointed out in this paper.

Most important, in this paper, we identify a special non-coplanar asymmetric Bragg diffraction scattering geometry, and show that in this case crystals can function as high-reflectance ($\sim 15\%$) broadband (~ 0.5 eV) diffraction gratings featuring dispersion rates ($\mathcal{D} \simeq 30$ µrad meV^{-1} at ~ 1 keV) that are two orders of magnitude larger than what is possible with man-made gratings. Examples of large-dispersion-rate crystal diffraction gratings are presented operating near the 930 eV L_3 absorption edge in Cu and of the 2.838 keV L_3-edge in Ru. Application of such gratings may open up new opportunities to design and implement monochromators and spectrometers with spectral resolution that is two orders of magnitude higher ($\Delta E \simeq 0.1$–1 meV) in the soft X-ray regime. This is especially attractive in view of the rapid recent advances in RIXS spectroscopy in the soft X-ray domain calling for further improvements in spectral resolution. However, the application of such gratings could be broader, not necessarily limited to RIXS spectroscopy.

2. Angular dispersion in Bragg diffraction

X-ray Bragg diffraction from a crystal alone does not yet guarantee the grating effect of angular dispersion. Diffracting atomic planes that are parallel to the crystal surface [see Fig. 1(*a*)] ensure high X-ray reflectivity from a crystal in Bragg diffraction, but zero angular dispersion. The diffracting atomic planes at a nonzero (asymmetry) angle η to the crystal surface [see Figs. 1(*b*) and 2(*a*)] ensure both high Bragg reflectivity and a periodic modulation of the electron density along the surface, with the latter resulting in the grating effect of the angular dispersion (Shvyd'ko, 2004). The larger the asymmetry angle, the shorter the period of the 'diffraction grating' and the larger the expected angular dispersion rate.

Here, we study asymmetric Bragg diffraction in coplanar scattering geometry [shown in Fig. 1(*b*)], and in non-coplanar scattering geometry [presented in Fig. 2(*a*)] to reveal the case featuring both the largest angular dispersion rate and the largest Bragg reflectivity, along with the largest spectral bandwidth. The performance of crystals as soft X-ray diffraction gratings will be presented on examples of crystals that feature sufficiently large lattice parameters, such as beryl ($Al_2Be_3Si_6O_{18}$).

In the coplanar asymmetric scattering geometry, the scattering plane composed by wavevectors $\mathbf{K}_0$ and $\mathbf{K}_H$ of the incident and of the diffracted X-ray photons coincide with the dispersion plane composed of the diffraction vector $\mathbf{H}$ and the internal crystal normal $\hat{\mathbf{z}}$ [shown in Fig. 1(*b*)]. In a general case of non-coplanar scattering geometry they are not parallel. In the particular non-coplanar case shown in Fig. 2(*a*), the scattering and dispersion planes are perpendicular to each other.

Momentum conservation in Bragg diffraction,

$$\mathbf{K}_H = \mathbf{K}_0 + \tilde{\mathbf{H}}, \qquad \tilde{\mathbf{H}} = \mathbf{H} + \Delta_{\mathbf{H}}\mathbf{z}, \qquad (1)$$

includes the total momentum transfer $\tilde{\mathbf{H}}$, that is a sum of diffraction vector $\mathbf{H}$ and of an additional momentum transfer
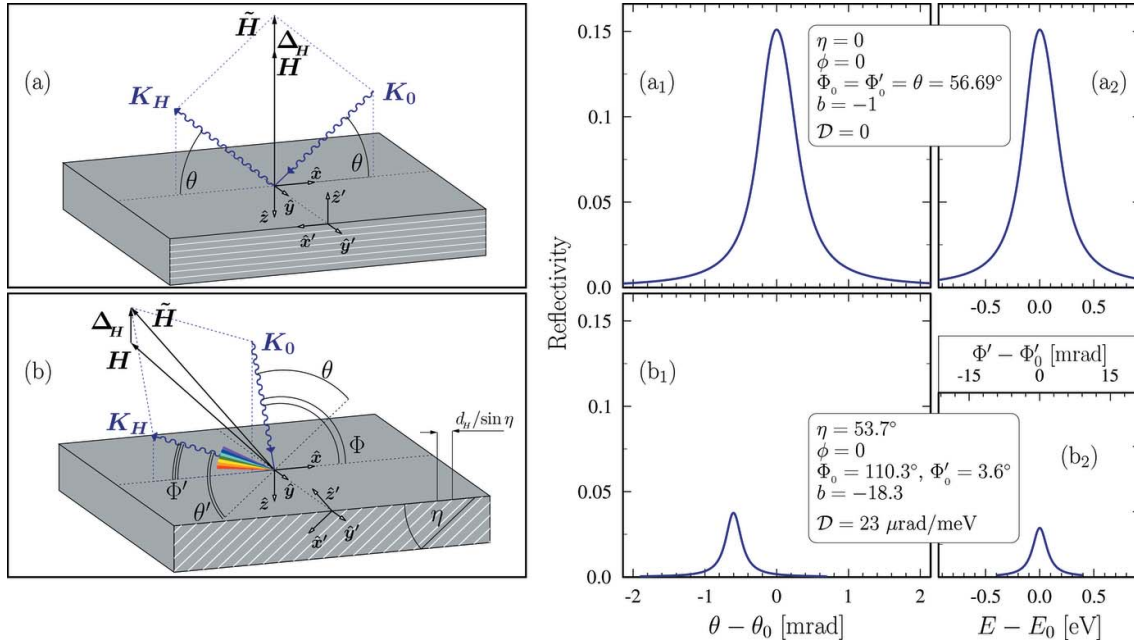
Figure 1
Performance of crystals as soft-X-ray diffraction gratings. X-ray reflectivity and dispersion rate $\mathcal{D}$ in Bragg diffraction from crystals in various scattering geometries (a)–(b) calculated as a function of the glancing angle of incidence θ to the Bragg diffracting atomic planes (a_1)–(b_1) and of X-ray photon energy E (a_2)–(b_2). (a) Symmetric geometry with diffracting planes (white parallel lines) parallel to the crystal surface. (b) Asymmetric coplanar diffraction with diffracting atomic planes at an asymmetry angle η to the entrance surface, and with the scattering plane $(\mathbf{K}_0, \mathbf{K}_H)$ parallel to the dispersion plane $(\mathbf{H}, \hat{\mathbf{z}})$. The θ-angle dependences of the Bragg reflectivity from the $(10\bar{1}0)$ atomic planes of a beryl crystal $(Al_2Be_3Si_6O_{18})$ are calculated for a photon energy $E_0 = 930$ eV, and mapped on the angular scale relative to $\theta_0 = 56.66°$, the angular position of the peak reflectivity in symmetric Bragg diffraction (a). Each energy E dependence is calculated at θ fixed at the peak reflectivity value. The angular dispersion fan [indicated by colors in (b)] is in the dispersion plane. The largest $\mathcal{D}$ is at the largest η.

Δ_H directed along $\mathbf{z}$. This is a small but essential term for the angular dispersion effect, which originates from refraction at the vacuum–crystal interface (Shvyd'ko, 2004). It can be determined from the photon energy E conservation $|\mathbf{K}_H| = |\mathbf{K}_0| = K = E/\hbar c$ as

$$\Delta_H = K\left[-\gamma_H \pm \left(\gamma_H^2 - \alpha\right)^{1/2}\right], \qquad (2)$$

where

$$\gamma_H = \frac{(\mathbf{K}_0 + \mathbf{H})\,\mathbf{z}}{K_0} = \gamma_0 - \frac{H}{K}\cos\eta, \qquad \gamma_0 = \frac{\mathbf{K}_0\mathbf{z}}{K_0} \qquad (3)$$

are direction cosines of $\mathbf{K}_0 + \mathbf{H}$ and of $\mathbf{K}_0$ with respect to z, respectively; the dimensionless parameter

$$\alpha = \frac{H}{K}\left(\frac{H}{K} - 2\sin\theta\right), \qquad (4)$$

measures the deviation from Bragg's law $2K\sin\theta = H$; and θ is a glancing angle of incidence to the reflecting atomic planes. The sign in equation (2) is chosen such that $\Delta_H = 0$ if $\alpha = 0$. In the Bragg-case reflection geometry considered here, in which $\gamma_H < 0$, the sign in equation (2) is negative (as opposed to the Laue-case transmission geometry in which $\gamma_H > 0$).

The angular dispersion rate $\vec{\mathcal{D}} = d\mathbf{u}_H/dE$ is calculated using equations (1)–(4) as a variation with photon energy E (or equivalently with K) of the direction of the normalized wavevector $\mathbf{u}_H = \mathbf{K}_H/K$ of the diffracted photon assuming *a fixed direction of the incident photon wavevector* $\mathbf{K}_0$,

$$\vec{\mathcal{D}} = -\frac{\mathbf{H}}{K\,E} + \frac{2\sin^2\theta}{E\,\gamma_H'}\hat{\mathbf{z}}, \qquad (5)$$

$$\gamma_H' = \pm\left(\gamma_H^2 - \alpha\right)^{1/2} = \frac{\mathbf{K}_H\mathbf{z}}{K_0}, \qquad (6)$$

where γ_H' is the cosine of the angle between the vacuum wavevector $\mathbf{K}_H$ and the surface normal $\hat{\mathbf{z}}$. In the Bragg-case scattering geometry considered here, $\gamma_H' < 0$. Alternatively, γ_H' can be expressed as $\gamma_H' = -\sin\Phi'$ through the sine of an angle Φ' between $\mathbf{K}_H$ and the crystal surface. Similarly, $\gamma_0 = \sin\Phi$ can be expressed as the sine of an angle Φ between $\mathbf{K}_0$ and the crystal surface. The angles Φ' and Φ are related to each other by

$$\begin{aligned}(\sin\Phi')^2 &= (\Psi - \sin\Phi)^2 - \alpha, \\ \Psi &= (H/K)\cos\eta,\end{aligned} \qquad (7)$$

which follows from equations (3) and (6).

Combining equations (5) and (6) we obtain

$$\vec{\mathcal{D}} = -\frac{2\sin\theta}{E}\left(\frac{\sin\theta}{\sin\Phi'}\hat{\mathbf{z}} + \hat{\mathbf{z}}'\right). \qquad (8)$$

According to equation (8), the angular dispersion rate vector $\vec{\mathcal{D}}$ is always in the dispersion plane $(\hat{\mathbf{z}}, \hat{\mathbf{z}}')$ (Shvyd'ko, 2004). The largest magnitude $|\vec{\mathcal{D}}|$ of the angular dispersion rate is achieved at grazing emergence, when the wavevector $\mathbf{K}_H$ makes a small angle, $\Phi' \ll 1$, with the crystal surface.

In this extreme case, equation (8) simplifies to
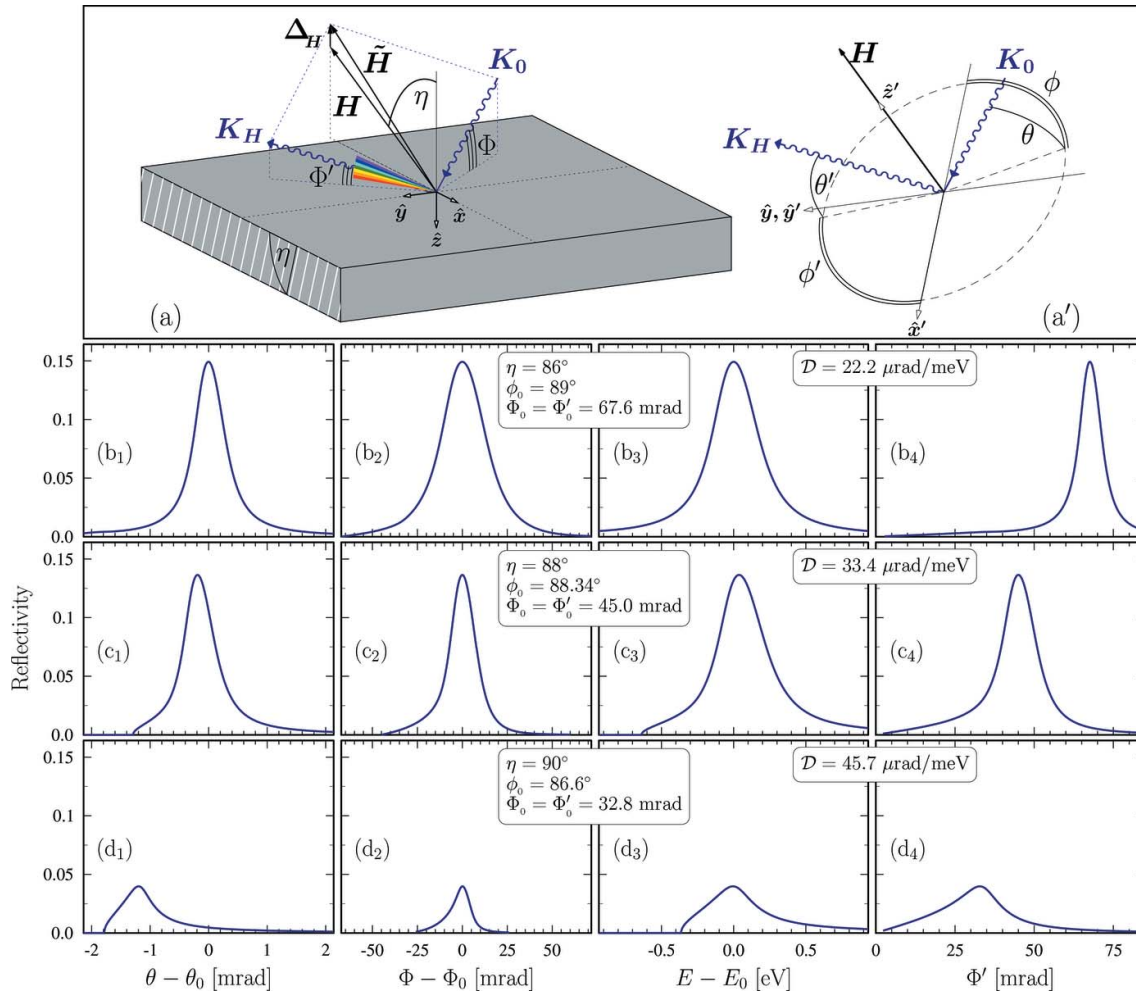
Figure 2
Reflectivity and angular dispersion $\mathcal{D}$ of soft-X-ray diffraction gratings similar to those in Fig. 1, but calculated in *non-coplanar* asymmetric scattering geometry as presented in panels (*a*) and (*a'*). In the non-coplanar case, the scattering plane $(\mathbf{K}_0, \mathbf{K}_H)$ and the dispersion plane $(\mathbf{H}, \hat{\mathbf{z}})$ are no longer parallel. They are perpendicular in the case presented here. The Bragg reflectivity dependences shown in rows (*b*)–(*d*) are calculated for different asymmetry angles η. In each (*b*), (*c*) or (*d*) case, the azimuthal angle of incidence $\phi = \phi_0$ [see Shvyd'ko (2004) for the definition] is chosen such that $\Phi_0 = \Phi_0'$, where Φ_0 and Φ_0' are the angles between the crystal surface and $\mathbf{K}_0$ and $\mathbf{K}_H$, respectively, as measured at the peak reflectivity. The Bragg reflectivities at fixed photon energy $E = E_0 = 930$ eV and $\phi = \phi_0$ as a function of θ and Φ are shown in (b_1)–(d_1) and (b_2)–(d_2), respectively. Bragg reflectivities calculated as a function of E with θ fixed at the peak reflectivity values are presented in (b_3), (c_3), and (d_3), while graphs in (b_4), (c_4), and (d_4) show the reflectivity mapped on Φ' that changes simultaneously with E due to angular dispersion. Largest $\mathcal{D}$ is at smallest Φ_0 and Φ_0'.

$$\vec{\mathcal{D}} \simeq -\hat{\mathbf{z}} \, |\mathcal{D}|, \qquad |\mathcal{D}| \simeq \frac{1}{E} \frac{2 \sin^2 \theta}{\sin \Phi'}, \qquad (9)$$

with the dispersion rate vector $\vec{\mathcal{D}}$ perpendicular to the crystal surface.[1] In the angular dispersion fan, photons with higher energies propagate at larger angles Φ' to the surface, as indicated by the violet color in Figs. 1(*b*) and 2(*a*). Using equation (9), we estimate $\mathcal{D} > 20$ μrad meV^{-1} for $E = 930$ eV, assuming $\Phi' \lesssim 60$ mrad,[2] the values, which are two orders of magnitude larger than those possible using manmade diffraction gratings (Ghiringhelli *et al.*, 2006; Strocov *et al.*,

2010; Chaix *et al.*, 2017; Brookes *et al.*, 2018; Bisogni, 2019; Warwick *et al.*, 2014; Chuang *et al.*, 2017; Lai *et al.*, 2014; Zhou, 2019; Dvorak *et al.*, 2016; Voronov *et al.*, 2014, 2015).

3. Soft X-ray crystal gratings

The theory presented in the previous section brings us to a conclusion that very large dispersion rates $\mathcal{D}$ can be achieved in asymmetric Bragg diffraction from crystals in various scattering geometries, provided the grazing reflection angle $\Phi' \ll 1$. However, a critical question is whether the high reflectivity and spectral bandwidth of the Bragg reflection can be simultaneously retained. Let us consider some particular cases, beginning with the conceptually simplest one of the coplanar scattering geometry.

Figs. 1(*a*) and 1(*b*) show schematics of Bragg diffraction from a crystal in the symmetric ($\eta = 0$) and asymmetric ($\eta \neq 0$)

---

[1] The angular dispersion rate given by equation (9) is equivalent to the angular dispersion rate $\mathcal{D} = (g \, hc)/(E^2 \sin \Phi')$ of a grating with a groove density g (see Appendix A), which is $g = \sin \theta / d_H$ in our case [see Fig. 1(*b*)] where the crystal 'grating' is determined by the interplanar distance $d_H = 2\pi/H$ between the diffracting atomic planes and incidence angle θ.

[2] The Φ' value is chosen here to be as small as possible, but larger than a critical angle of ~33 mrad for 930 eV photons in beryl.

coplanar scattering geometries, respectively. Figs. 1(a_1) and 1(b_1) show the Bragg reflection profiles related to these scattering geometries as a function of incidence angle θ at a fixed photon energy $E = E_0 = 930$ eV in the $(10\bar{1}0)$ Bragg diffraction from a beryl crystal ($Al_2Be_3Si_6O_{18}$). Figs. 1(a_2) and 1(b_2) show the corresponding Bragg reflection profiles as a function of photon energy E, calculated with θ fixed at the peak reflectivity value.

In the symmetric scattering geometry, the reflection profiles are relatively broad with an angular acceptance of 0.6 mrad and an energy bandwidth of 0.37 eV, respectively, featuring about 15% reflectivity [see Figs. 1(a_1)–1(a_2)]. Although the Bragg reflectivity in this case is relatively low compared with the 80% to 90% reflectivity typical in the hard X-ray regime (because of high photoabsorption of the 930 eV photons), it is still larger than the typical diffraction gratings reflectivity of $\sim$5%, unless multilayer-coated blazed grating are used (Voronov *et al.*, 2014, 2015). The angular dispersion rate is, however, zero in the case of symmetric diffraction.

In contrast, a very large value of the dispersion rate, $\mathcal{D} \simeq 23$ µrad meV^{-1}, is achieved in strongly asymmetric diffraction with an asymmetry angle of $\eta = 53.7°$. In this case the reflected photons propagate at reflection angle Φ' varying with photon energy, with $\Phi'_0 = 63$ mrad ($3.6°$) at the reflectivity peak; see Fig. 1(b_2). The dispersion rate is two orders of magnitude larger than what is possible with man-made diffraction gratings at the same photon energy (Ghiringhelli *et al.*, 2006; Strocov *et al.*, 2010; Chaix *et al.*, 2017; Brookes *et al.*, 2018; Bisogni, 2019; Warwick *et al.*, 2014; Chuang *et al.*, 2017; Lai *et al.*, 2014; Zhou, 2019; Dvorak *et al.*, 2016). However, this comes at a high price of a factor of three reduced angular acceptance reduced to 0.24 mrad and of the energy bandwidth to 0.16 eV. The reflectivity is reduced even more, by a factor of four, to 3.9%.

The drastic reduction of the angular and spectral widths together with the Bragg reflectivity is due to the large change in the magnitude of the asymmetry factor, $b = \gamma_0/\gamma_H = -\sin\Phi/\sin\Phi'$. It changes from the favorable for the high-reflectivity value $b = -1$ in the symmetric scattering geometry, for which $\Phi = \Phi' = \theta = 56.66°$, to $b \simeq -18$ in the asymmetric scattering geometry considered here, for which $\Phi = \theta + \eta = 130.3°$ and $\Phi' = \theta - \eta = 3.6°$.

In the following, we show that asymmetric Bragg diffraction can also be realized featuring $b \simeq -1$ and ensuring not only

the large dispersion rates $\mathcal{D}$ as in Fig. 1(b_2) but also broad spectral widths together with high reflectivity, comparable with those of the symmetric case presented in Figs. 1(a_1)–1(a_2). This is achieved in a particular asymmetric non-coplanar scattering case, in which $\Phi \simeq \Phi'$ (quasi-symmetric case) [see Figs. 2(a)–2(a')].

Rows $x = b$, c, and d in Figs. 2(x_1)–2(x_4) show examples of the angular and spectral Bragg reflection profiles similar to those presented in Fig. 1. However, they are calculated in the non-coplanar 'quasi-symmetric' scattering geometry with values of $\Phi_0 \simeq \Phi'_0$ decreasing from (a) to (c). The details of the calculated profiles are explained in the caption of Fig. 2. Importantly, the Φ- and Φ'-dependences presented in Figs. 2(x_2) and 2(x_4) show mrad-broad angular acceptances in Φ and mrad-broad angular spread in Φ', respectively. The large angular spread in Φ' (calculated at fixed Φ) is due to large angular dispersion rate values growing to $\mathcal{D} > 33$ µrad meV^{-1} with decreasing values of $\Phi_0 \simeq \Phi'_0$. The Bragg reflectivity is as high and the reflection profiles are as broad as in the symmetric case; compare Figs. 2(x_1) and 2(x_3) with Figs. 1(a_1) and 1(a_2). Only when $\Phi_0 \simeq \Phi'_0 \simeq 33$ mrad becomes comparable with the critical angle and the two-beam Bragg diffraction transforms into the four-beam grazing-incidence diffraction (Afanas'ev & Melkonyan, 1983; Aleksandrov *et al.*, 1984; Bushuev & Oreshko, 2001) does the reflectivity drop [see Figs. 2(d_1)–2(d_4)].

Figs. 3(a_1)–3(a_4) show another interesting case of non-coplanar 'quasi-symmetric' Bragg diffraction. Here, the (111) Bragg reflection of 2.838 keV X-rays from a Si crystal features a $\mathcal{D} = 13$ µrad meV^{-1} dispersion rate. The optical element with such a large dispersion rate and a >60%-reflectivity can be used as an efficient diffraction grating in a Ru L_3-edge RIXS spectrometer to ensure meV or even sub-meV resolution.

No doubt Si-based diffraction gratings will perform well because nearly flawless synthetic crystals are available. However, Si crystals are not applicable in the photon spectral range below 2 keV, because they have a relatively small crystal lattice parameter. Crystals with larger lattice parameters are known and have been used in soft-X-ray Bragg diffraction monochromators (Johnson, 1983; Feldhaus *et al.*, 1986; Kortboyer *et al.*, 1989; Xu *et al.*, 1998; Wang *et al.*, 2012). Among them are beryl crystals ($Al_2Be_3Si_6O_{18}$), which can diffract photons with energies above 780 eV, KAP crystals diffracting
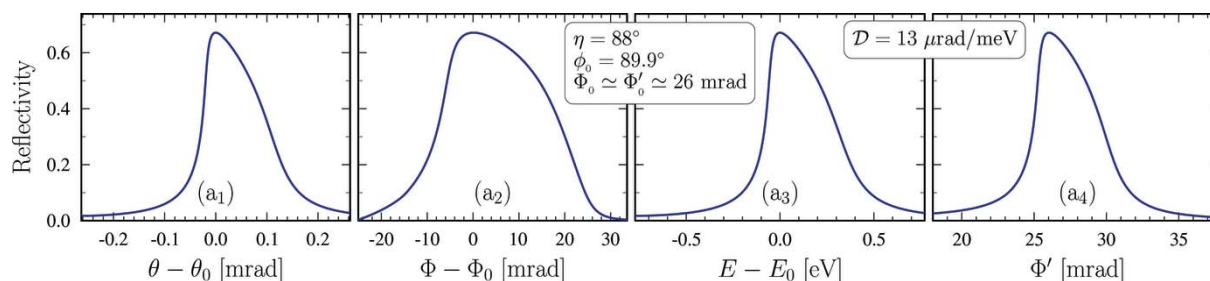
Figure 3
Reflectivity and angular dispersion $\mathcal{D}$ of X-rays in Bragg diffraction from the (111) atomic planes in Si crystal in non-coplanar asymmetric diffraction with asymmetry angle $\eta = 88°$ and $\theta_0 = 44.16°$, similar to those in Fig. 2, but calculated with photon energies in the vicinity of the Ru L_3-edge ($E_0 = 2.838$ keV).

above 600 eV, and others. However, because their quality is inferior it is of course a question of whether these crystals can perform appropriately as diffraction gratings. In Appendix B, we show that natural beryl crystal quality may be sufficient for them to be used as diffraction gratings in meV-resolution spectrometers.

4. Summary

In summary, we identified an asymmetric Bragg diffraction scattering geometry that ensures very high angular dispersion rates, along with high reflectivity and a large spectral reflection range of crystals in the soft X-ray regime. This is exemplified in a non-coplanar case, where the scattering and dispersion planes are perpendicular to each other, and X-rays propagate at very small but equal grazing angles of incidence and reflection to the crystal surface. The Bragg diffraction dispersion rates in the soft-X-ray regime can be more than two orders of magnitude larger than what is possible with man-made diffraction gratings. We note that crystal-based variable-line-spacing gratings can also be realized by introducing a temperature gradient along the crystal surface in the dispersion plane. All this opens new opportunities to design and implement soft X-ray RIXS spectrometers with spectral resolutions that are up to two orders of magnitude higher than what is currently possible, to further advance a very dynamic field of RIXS spectroscopy, and to make it competitive with inelastic neutron scattering. The application of such gratings could be broader, not necessarily limited to RIXS spectroscopy.

APPENDIX A
Diffraction grating dispersion rate and spectral resolution of soft-X-ray spectrometers

The variation of grating groove density $g(x)$ in a general case is represented as a polynomial (Warwick *et al.*, 2014),

$$g(x) = g_0 + g_1 x + g_2 x^2 + g_3 x^3. \quad (10)$$

The plane grating equation is

$$\sin \alpha + \sin \beta = m \lambda g_0 = m g_0 \frac{hc}{E}, \quad (11)$$

where $\alpha > 0$ and $\beta < 0$ are angles of incidence and diffraction, respectively; m is the diffraction order; λ is the wavelength; $E = hc/\lambda$ is the photon energy, and $hc = 1.2398$ eV μm.

The angular dispersion rate $\mathcal{D}$ (variation of β with E at fixed α) is

$$\mathcal{D} = \frac{d\beta}{dE} = -\frac{m g_0 hc}{E^2 \cos \beta}. \quad (12)$$

With the Au-coated grating parameters $g_0 = 5$ μm^{-1}, $\beta = -87.6°$, $m = -1$ provided by Warwick *et al.* (2014) the dispersion rate at $E = 930$ eV is $\mathcal{D} = 0.17$ μrad meV^{-1}. Gratings with similar dispersion rates were considered in application to state-of-the-art major soft X-ray RIXS spectrometers (Ghiringhelli *et al.*, 2006; Strocov *et al.*, 2010; Chaix *et al.*, 2017;

Brookes *et al.*, 2018; Bisogni, 2019; Warwick *et al.*, 2014; Chuang *et al.*, 2017; Lai *et al.*, 2014; Zhou, 2019; Dvorak *et al.*, 2016). The angular dispersion rates of the gratings based on Bragg-diffracting crystals discussed in this paper are about two orders of magnitude larger. This can be used to improve the spectral resolution of the soft-X-ray spectrometers by at least two orders of magnitude.

Contributions to the spectral resolution of a grating spectrometers are listed below, following Ghiringhelli *et al.* (2006).

Assuming unlimited detector resolution and a grating with no slope errors, the major contribution to the spectral resolution of the spectrometer is due to the secondary source size (on the sample) Δx_1 in the dispersion plane, which is

$$\Delta E_1 = \frac{\Delta x_1 \cos \alpha}{r_1} \frac{E^2}{m g_0 hc} = \frac{\Delta x_1}{r_1} \frac{1}{|\mathcal{D}|} \frac{\cos \alpha}{\cos \beta}. \quad (13)$$

Here, r_1 is a distance from the secondary source to the focusing grating. The right-hand side of equation (13) coincides with the spectral resolution of the Bragg-crystal-based grating spectrometer (Shvyd'ko, 2015); note that $\cos \alpha / \cos \beta$ has the same meaning as the asymmetry ratio $|b|$ in Bragg crystal optics.

If the monochromatic image size Δx_2 on the detector is smaller than the detector spatial resolution Δx_D, there is an additional detrimental contribution to the spectral resolution,

$$\Delta E_2 = \frac{\Delta x_D \cos \beta}{r_2} \frac{E^2}{m g_0 hc} = \frac{\Delta x_D}{r_2} \frac{1}{|\mathcal{D}|}. \quad (14)$$

Here, r_2 is a distance from the focusing grating to the pixel detector. In this case, the expression also coincides with a similar expression in Shvyd'ko (2015).

The slope error contribution σ (r.m.s.) to the spectral resolution is given by

$$\Delta E_3 = 2.35\sigma \left(1 + \frac{\cos \alpha}{\cos \beta}\right) \frac{1}{|\mathcal{D}|}. \quad (15)$$

The net spectral resolution ΔE is a sum of all contributions: $\Delta E = (\Delta E_1^2 + \Delta E_2^2 + \Delta E_3^2)^{1/2}$.

It is remarkable that

$$\Delta E_1 \propto \frac{1}{\mathcal{D}}, \quad \Delta E_2 \propto \frac{1}{\mathcal{D}}, \quad \Delta E_3 \propto \frac{1}{\mathcal{D}}, \quad \Delta E \propto \frac{1}{\mathcal{D}}. \quad (16)$$

In other words, a large value of the angular dispersion rate $\mathcal{D}$ is favorable for reducing detrimental contributions of each component and achieving the highest spectral resolution of the spectrometers.

APPENDIX B
Crystal quality of natural beryl: X-ray rocking-curve-imaging studies

Feasibility of the Bragg-diffraction soft-X-ray crystal dispersing elements (diffraction gratings) relies on the availability of crystals with a large crystal lattice parameter and good crystal quality. High-quality crystals such as silicon cannot diffract X-rays with photon energies below 2 keV. Crystals with larger
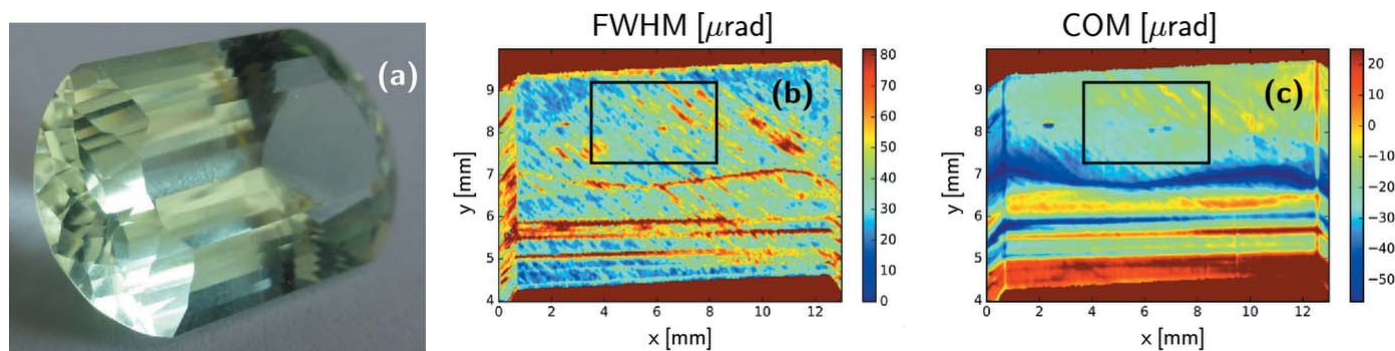
Figure 4
Photograph of a natural faceted beryl crystal (*a*) characterized by X-ray rocking curve imaging (*b*)–(*c*). The (0004) Bragg reflection color maps of the angular widths (FWHM) (*b*), and of the center of mass (COM) of the rocking curves (*c*).

lattice parameters are known and have been used in soft X-ray Bragg diffraction monochromators (Johnson, 1983; Feldhaus *et al.*, 1986; Kortboyer *et al.*, 1989; Xu *et al.*, 1998; Wang *et al.*, 2012). Among them are beryl crystals ($Al_2Be_3Si_6O_{18}$), which can diffract photons with energies above 780 eV; KAP crystals diffracting X-rays above 600 eV, and others. However, because of their inferior quality it is a question of whether they can perform appropriately as diffraction gratings.

A few natural beryl crystals were obtained from D Sarros Gems Limited (Geneva, IL, USA) to evaluate their Bragg-diffraction performance. Samples were selected in the (0001) orientation. Fig. 4(*a*) shows a photograph of one of the crystals, with lateral dimensions of ∼15 mm × 25 mm.

The selected beryl crystals were characterized with 8 keV X-rays by sequential X-ray Bragg diffraction topography, also known as rocking curve imaging (Lübbert *et al.*, 2000). This technique measures Bragg reflection images of a crystal with a pixel X-ray detector sequentially at different incidence angles to the Bragg reflecting atomic planes. The angular dependences of Bragg reflectivity (rocking curves) measured with each detector pixel are used to calculate Bragg reflection maps: first, a map of the angular widths [full width at half-maximum (FWHM)] of the rocking curves is calculated, shown as a color map in Fig. 4(*b*), and, second, a color map of the center of mass (COM) of the rocking curves shown in Fig. 4(*c*). The microscopic defect structure can be derived from the Bragg reflection FWHM maps. The mesoscopic and macroscopic crystal strain and Bragg planes slope errors can be best evaluated from the COM maps.

We used a sequential X-ray diffraction topography setup at the X-ray Optics Testing 1-BM Beamline at Argonne's Advanced Photon Source (Stoupin *et al.*, 2016). The setup enables rocking-curve mapping with a submicroradian angular and 13 µm spatial resolution, limited by the detector pixel size. The setup employed a close-to-nondispersive double-crystal Si(220)–beryl(0004) arrangement with the first asymmetrically cut high-quality silicon conditioning crystal (Bragg's angle $\theta_{220} = 23.8°$), and the second beryl crystal under investigation (Bragg's angle $\theta_{0004} = 19.7°$). The expected theoretical value of the 0004 Bragg reflection width in beryl is $\Delta\theta_{0004} = 12$ µrad (FWHM). Scales on the *x*- and *y*-axis in Figs. 1(*b*)–1(*c*)

correspond to the detector coordinates. The diffraction plane goes through the *y*-axis. The crystal therefore appears to be contracted by a factor of $\sin\theta_{0004} = 0.3$ in the *y*-direction. The maps were calculated using a dedicated code (Stoupin, 2015).

The reflection maps show that crystal quality varies substantially. They also reveal a layered crystal structure, which indicates that the crystal grew in the earth's crust under varying conditions over time. The inclined parallel lines result from crystal polishing.

In the region indicated by the black rectangle, which is about 4 mm (*x*) × 6 mm (*y*) (sufficient in size for our application), the quality is relatively homogeneous. The averaged over the selected area reflection width is $\Delta\theta = 23$ µrad (FWHM) and the averaged peak variation is $\sigma_{COM} = 4$ µrad. These results clearly show that the crystals are not perfect. However, these results are promising, because the measured values of $\Delta\theta$ and σ_{COM} have to be compared with the reflection width and dispersion rates expected in Bragg diffraction of 930 eV X-rays, which are 0.6 mrad and 22 µrad meV^{-1}, respectively. Because the expected values are larger than the measured ones, the results of these studies show that the quality of natural beryl crystals may be sufficient for use as soft-X-ray crystal diffraction gratings.

We note also that radiation damage of beryl was reported previously when it was used in an X-ray monochromator under high-heat-load conditions (Feldhaus *et al.*, 1986). This should not be a problem if beryl crystals are used as analyzers or diffraction gratings (Wang *et al.*, 2012). The grazing-incidence geometry foreseen for the beryl's application as a diffraction grating should be favorable to mitigate the radiation load. In addition, use of cryogenic cooling may improve thermal conductivity and reduce radiation damage on the monochromator crystal.

research papers

References

Afanas'ev, A. M. & Melkonyan, M. K. (1983). *Acta Cryst.* A**39**, 207–210.

Aleksandrov, P. A., Afanasiev, A. M. & Stepanov, S. A. (1984). *Phys. Status Solidi A*, **86**, 143–154.

Bisogni, V. (2019). *11th International Conference on Inelastic X-ray Scattering (IXS2019)*, 23–28 June 2019, Stony Brook, NY, USA (https://www.bnl.gov/ixs2019/files/talks/wednesday/Valentina Bisogni.pdf).

Braicovich, L., van den Brink, J., Bisogni, V., Sala, M. M., Ament, L. J. P., Brookes, N. B., De Luca, G. M., Salluzzo, M., Schmitt, T., Strocov, V. N. & Ghiringhelli, G. (2010). *Phys. Rev. Lett.* **104**, 077002.

Brookes, N., Yakhou-Harris, F., Kummer, K., Fondacaro, A., Cezar, J., Betto, D., Velez-Fort, E., Amorese, A., Ghiringhelli, G., Braicovich, L., Barrett, R., Berruyer, G., Cianciosi, F., Eybert, L., Marion, P., van der Linden, P. & Zhang, L. (2018). *Nucl. Instrum. Methods Phys. Res. A*, **903**, 175–192.

Bushuev, V. A. & Oreshko, A. P. (2001). *Phys. Solid State*, **43**, 941–948.

Chaix, L., Ghiringhelli, G., Peng, Y. Y., Hashimoto, M., Moritz, B., Kummer, K., Brookes, N. B., He, Y., Chen, S., Ishida, S., Yoshida, Y., Eisaki, H., Salluzzo, M., Braicovich, L., Shen, Z.-X., Devereaux, T. P. & Lee, W.-S. (2017). *Nat. Phys.* **13**, 952–956.

Chuang, Y.-D., Shao, Y.-C., Cruz, A., Hanzel, K., Brown, A., Frano, A., Qiao, R., Smith, B., Domning, E., Huang, S.-W., Wray, L. A., Lee, W.-S., Shen, Z.-X., Devereaux, T. P., Chiou, J.-W., Pong, W.-F., Yashchuk, V. V., Gullikson, E., Reininger, R., Yang, W., Guo, J., Duarte, R. & Hussain, Z. (2017). *Rev. Sci. Instrum.* **88**, 013110.

Chumakov, A. I., Shvyd'ko, Yu., Sergueev, I., Bessas, D. & Rüffer, R. (2019). *Phys. Rev. Lett.* **123**, 097402.

Dean, M. P. M., Dellea, G., Springell, R. S., Yakhou-Harris, F., Kummer, K., Brookes, N. B., Liu, X., Sun, Y.-J., Strle, J., Schmitt, T., Braicovich, L., Ghiringhelli, G., Božović, I. & Hill, J. P. (2013). *Nat. Mater.* **12**, 1019–1023.

Dvorak, J., Jarrige, I., Bisogni, V., Coburn, S. & Leonhardt, W. (2016). *Rev. Sci. Instrum.* **87**, 115109.

Feldhaus, J., Schafers, F. & Peatman, W. (1986). *Proc. SPIE*, **0733**, 242–247.

Ghiringhelli, G., Piazzalunga, A., Dallera, C., Trezzi, G., Braicovich, L., Schmitt, T., Strocov, V. N., Betemps, R., Patthey, L., Wang, X. & Grioni, M. (2006). *Rev. Sci. Instrum.* **77**, 113108.

Johnson, R. L. (1983). *Handbook on Synchrotron Radiation*, Vol. 1A, pp. 173–260. Amsterdam: North-Holland.

Kortboyer, S., Goedkoop, J., De Groot, F. M. F., Grioni, M., Fuggle, J. & Petersen, H. (1989). *Nucl. Instrum. Methods Phys. Res. A*, **275**, 435–441.

Lai, C. H., Fung, H. S., Wu, W. B., Huang, H. Y., Fu, H. W., Lin, S. W., Huang, S. W., Chiu, C. C., Wang, D. J., Huang, L. J., Tseng, T. C., Chung, S. C., Chen, C. T. & Huang, D. J. (2014). *J. Synchrotron Rad.* **21**, 325–332.

Le Tacon, M., Ghiringhelli, G., Chaloupka, J., Sala, M. M., Hinkov, V., Haverkort, M. W., Minola, M., Bakr, M., Zhou, K. J., Blanco-Canosa, S., Monney, C., Song, Y. T., Sun, G. L., Lin, C. T., De Luca, G. M., Salluzzo, M., Khaliullin, G., Schmitt, T., Braicovich, L. & Keimer, B. (2011). *Nat. Phys.* **7**, 725–730.

Lübbert, D., Baumbach, T., Härtwig, J., Boller, E. & Pernot, E. (2000). *Nucl. Instrum. Methods Phys. Res. B*, **160**, 521–527.

Michette, A. (1986). *Optical Systems for Soft X-rays.* Berlin: Springer.

Schlappa, J., Wohlfeld, K., Zhou, K. J., Mourigal, M., Haverkort, M. W., Strocov, V. N., Hozoi, L., Monney, C., Nishimoto, S., Singh, S., Revcolevschi, A., Caux, J.-S., Patthey, L., Rønnow, H. M., van den Brink, J. & Schmitt, T. (2012). *Nature*, **485**, 82–85.

Shvyd'ko, Yu. (2004). *X-ray Optics – High-Energy-Resolution Applications*, Vol. 98 of *Optical Sciences.* Berlin: Springer.

Shvyd'ko, Yu. (2015). *Phys. Rev. A*, **91**, 053817.

Shvyd'ko, Yu., Stoupin, S., Shu, D., Collins, S. P., Mundboth, K., Sutter, J. & Tolkiehn, M. (2014). *Nat. Commun.* **5**, 4219.

Shvyd'ko, Yu. V., Lerche, M., Kuetgens, U., Rüter, H. D., Alatas, A. & Zhao, J. (2006). *Phys. Rev. Lett.* **97**, 235502.

Stoupin, S. (2015). *Python-DTXRD*, https://www1.aps.anl.gov/science/scientific software/dtxrd.

Stoupin, S., Shvyd'ko, Yu., Trakhtenberg, E., Liu, Z., Lang, K., Huang, X., Wieczorek, M., Kasman, E., Hammonds, J., Macrander, A. & Assoufid, L. (2016). *AIP Conf. Proc.* **1741**, 050020.

Strocov, V. N., Schmitt, T., Flechsig, U., Schmidt, T., Imhof, A., Chen, Q., Raabe, J., Betemps, R., Zimoch, D., Krempasky, J., Wang, X., Grioni, M., Piazzalunga, A. & Patthey, L. (2010). *J. Synchrotron Rad.* **17**, 631–643.

Voronov, D. L., Goray, L. I., Warwick, T., Yashchuk, V. V. & Padmore, H. A. (2015). *Opt. Express*, **23**, 4771–4790.

Voronov, D. L., Warwick, T. & Padmore, H. A. (2014). *Opt. Lett.* **39**, 6134–6137.

Wang, H., Dhesi, S. S., Maccherozzi, F. & Sawhney, K. J. S. (2012). *J. Appl. Phys.* **111**, 123117.

Warwick, T., Chuang, Y.-D., Voronov, D. L. & Padmore, H. A. (2014). *J. Synchrotron Rad.* **21**, 736–743.

Xu, C., Zhao, W., Pan, G., Liu, Y., Wu, G., Li, H. & Zhao, D. (1998). *Nucl. Instrum. Methods Phys. Res. A*, **410**, 293–296.

Zhou, K. (2019). *RIXS beamline at the Diamond Light Source*, https://www.diamond.ac.uk/Beamlines/Spectroscopy/I21.html.